Truncation Error Study on Near Field Antenna Characteristics using Compressive Sensing

M. Salucci, N. Anselmi, and A. Massa

2024/05/03

Contents

1 Cylindrical Measurement set-up

1.1 Fixed measurement step $\Delta_{\mathbf{z}}^{\mathbf{meas}} = 1\,[\lambda]$ and different number of measurement points (M)

For the performed analysis:

- the measurement points are distributed in a cylindrical surface place at a radial distance $\rho_{int} = \rho_{meas} = \rho = 5\,[\lambda]$ away from the *AUT* which is placed along the $z-$axis;
- the employed *AUT* is characterized by a magnitude failure and phase shift affecting the 2^{nd} row ($\nu^{(2)} = 0.43$, $\gamma^{(2)} = \frac{\pi}{3}$) and the considered failure ranges to build the over-complete basis are :$\nu^{(s)} \in [0.0,\, 1.0]\,,\ F^{(s)} = 7$ and $\gamma^{(s)} \in [-\pi,\, \frac{\pi}{2}]\,,\ P^{(s)} = 7$. All the main parameters used for the simulations are listed below:

Parameters

Gold Antenna (Without Defects)

- Geometry : Planar array of microstrip patches on the (x, y) plane;
- Working Frequency : $f = 3.6\,[GHz]$ ($\lambda = 83.27 \times 10^{-3}\,[m]$ in free space);
- Substrate (PEC-backed) :
  - Dimensions : infinite;
  - Relative Permittivity : $\varepsilon_{r,sub} = 4.7$;
  - Loss Tangent : $tan\,\delta_{sub} = 0.014$;
  - Thickness : $h_{sub} = 0.019\,[\lambda]\ (1.6\,[mm])$;
- Microstrip patches :
  - Dimensions : $l_x \approx 0.22\,[\lambda]\ (18.16\ [mm]),\ l_y \approx 0.33\,[\lambda]\ (27.25\ [mm])$;
  - Feeding : pin-fed;
- Spacing between elements : $d_x = d_y = \frac{\lambda}{2}$;
- Number of elements in each row : $N_y = 2$;
- Number of elements in each column : $N_z = 6$;
- Total number of elements : $N = (N_y \times N_z) = 12$;
- Total size of the antenna : $L_y = 1\,[\lambda],\ L_y = 3\,[\lambda]$;
- Element excitations : $w_n^{(s)} = 1.0 + j0.0,\ n = 1, ..., N^{(s)},\ s = 1, ..., S$;

Antenna Under Test (AUT - With Defects)

1. Failures of the excitation magnitude of the 2^{nd} row;

    - Failure factor of the elements in the 2^{nd} row $(s = 2)$: $\nu^{(2)} = 0.43$;

2. Failures of the excitation phase of the 2^{nd} row;

    - Phase shift of the elements in the 2^{nd} row $(s = 2)$: $\gamma^{(2)} = \frac{\pi}{3}\,[rad]$;

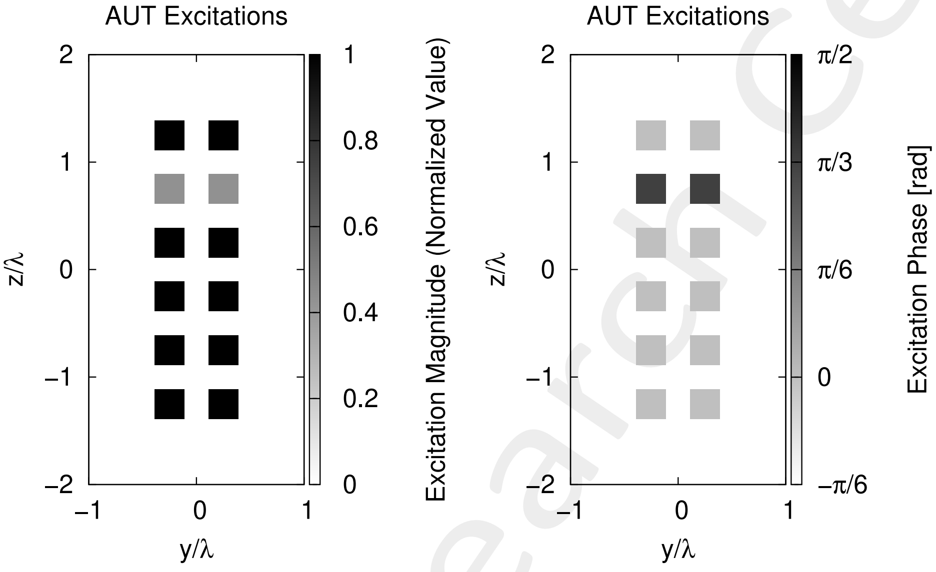

(a) (b)

Figure 1: (a) Magnitude of the element excitations in the *AUT* ($\nu^{(2)} = 0.43$), (b) phase of the element excitations in the *AUT* ($\gamma^{(2)} = \frac{\pi}{3}\,[rad]$).

Measurement-by-Design Technique

- Number of generated bases : $B = 12$;
- Bases $b = 1, ..., 6$: magnitude failures in each row $(s = 1, ..., 6)$
    - Failure factor of the elements : $\nu^{(s)} \in [0.0,\ 1.0],\ \ s = 1, ..., 6$;
    - Number of simulated failure factors : $F^{(s)} = 7,\ s = 1, ..., 6$;
- Bases $b = 7, ..., 12$: phase failures in each row $(s = 1, ..., 6)$
    - Phase shift of the elements : $\gamma^{(s)} \in [-\pi,\ \frac{\pi}{2}]\,[rad],\ \ s = 1, ..., 6$;
    - Number of simulated phase shifts: $P^{(s)} = 7,\ \ s = 1, .., 6$;
- Threshold on the singular values magnitude (normalized) : $\eta = -40\,[dB]$;
- Total number of simulated AUT configurations : $K = S \times (F^{(s)} + P^{(s)}) = 6 \times (7 + 7) = 84$;

Dimension of the Over-Complete Basis

The dimension of the over-complete basis is

$$Q = 24$$

This number is given by the sum of the vectors belonging to the two considered bases:

1. Magnitude failures : $Q_1, ..., Q_6 = 2$;
2. Phase failures : $Q_7, ..., Q_{12} = 2$.

Alternative (*BCS*) MbD parameters

- Toleration factor for *BCS* solver: $Tolerance = 1 \times 10^{-8}$;
- Initial noise variance for *BCS* solver: $\eta_0^{opt} = 5 \times 10^{-4}$. This values have been obtained as a result of a calibration procedure (see following Result section);

Noise

- SNR on the measured data : $SNR = \{50;\ 40;\ 30;\ 20;\ 10\}\ [dB]$;
- Noise seed : $Noise\_Seed = 1$.

Measurement Set-Up (Cylindrical)

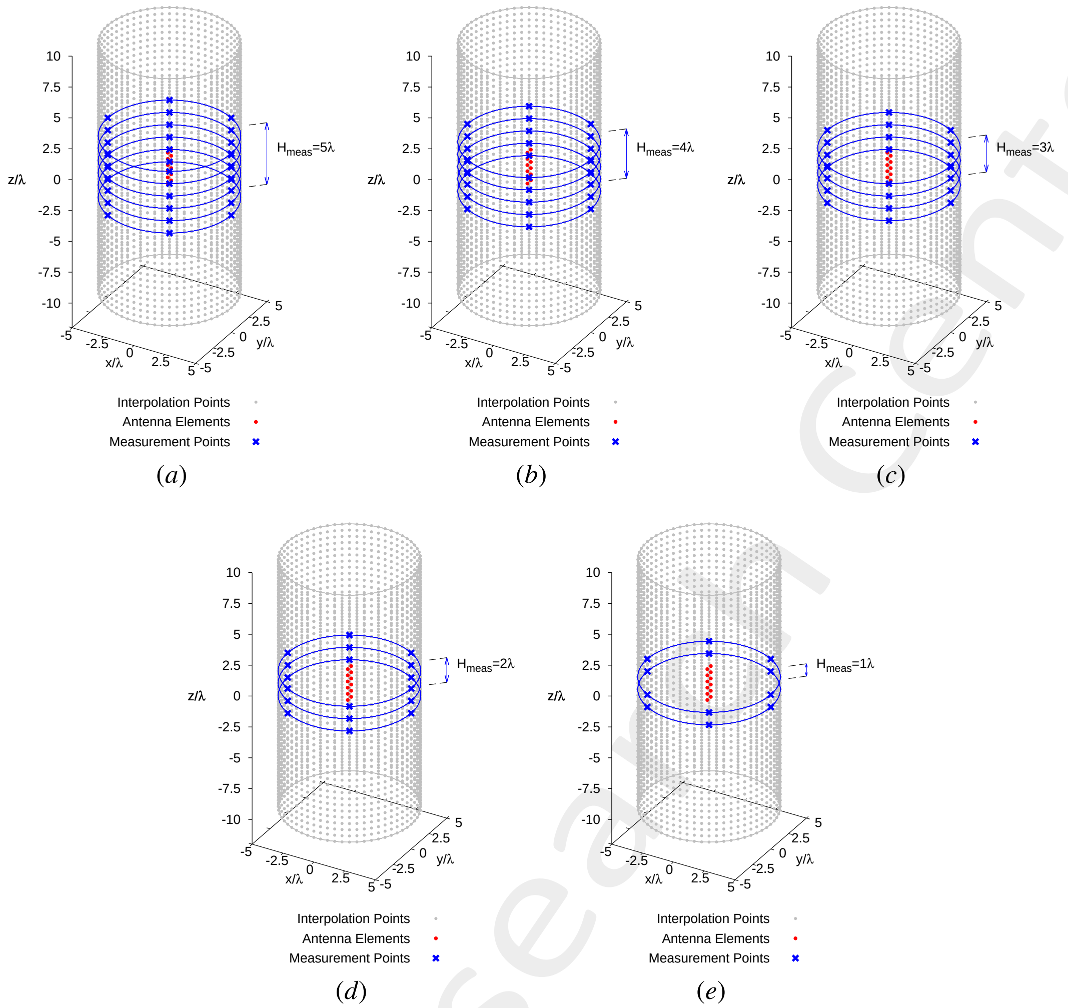

Figure 2: Disposition of the interpolation points ($T = 2501$) and of the measurement points (M) in the near-field region of the *AUT*.

- Type of measurements : near-field;
- Interpolation points :
  - Height of the interpolation region : $H_{int} = 20\,[\lambda]$;
  - Radius of the interpolation region : $R = 5\,[\lambda]$;
  - Number of points : $T = (T_{\varphi} \times T_z) = (61 \times 41) = 2501$;
  - Coordinates : $\rho_t \in R\,,\ \varphi_t \in [-180,\,180]\,[deg],\ z_t \in [-10,\,10]\,[\lambda],\ t = 1, ..., T$;
  - Interpolation step : $\Delta_z^{int} = 0.5\,[\lambda],\ \Delta_{\varphi}^{int} = 6\,[deg]$;
- Measurement points :
  - Height of the measurement region : $H_{meas} \in [1,\,5]\,[\lambda]$;
  - Radius of the interpolation region : $R = 5\,[\lambda]$;
  - Number of points : $M = (M_{\varphi} \times M_z)$;

$H_{meas}\,[\lambda]$	$\Delta_z^{meas}\,[\lambda]$	$\Delta_\varphi^{meas}\,[deg]$	M_z	M_φ	M
1	1	60	2	6	12
2	1	60	3	6	18
3	1	60	4	6	24
4	1	60	5	6	30
5	1	60	6	6	36

Table I: Measurement configurations.

Results

Calibration of the initial noise variance (η_0) for *BCS-MbD*

In order to find the best value for the initial noise variance value (η_0^{opt}), the *BCS* version of the *MbD* has been run considering the following parameter values :

- Measurement points :
  - Height of the measurement region : $H_{meas} = 1\,[\lambda]$;
  - Radius of the interpolation region : $R = 5\,[\lambda]$;
  - Number of points : $M = (M_\varphi \times M_z) = (2 \times 6) = 12$;
- $\eta_0 = [10^{-9}, 5{\times}10^{-9}, 10^{-8}, 5{\times}10^{-8}, 10^{-7}, 5{\times}10^{-7}, 10^{-6}, 5{\times}10^{-6}, 10^{-5}, 5{\times}10^{-5}, 10^{-4}, 5{\times}10^{-4}, 10^{-3}, 5\times 10^{-3}, 10^{-2}, 5 \times 10^{-2}, 10^{-1}, 5 \times 10^{-1}, 1, 5, 10]$;
- $SNR = [60, 50, 40, 30, 20]$;
- Noise seed : $Noise\_Seed = 1$.

The best value has been computed as the minimum mean near-field error over the considered *SNR* values for each η_0; in formula:

$$\eta_0^{opt} = min_{\eta_0^{(i)}} \left\{ \frac{\sum_{j=1}^{N_{SNR}} \Xi^{(j)}_{AUT,\eta_0^{(i)}}}{N_{SNR}} \right\} \tag{1}$$

where

- η_0^i is the $i-th$ considered η_0 value;
- $\Xi^{(j)}_{AUT,\eta_0^{(i)}}$ is the near field error obtained considering the $i-th$ value of η_0 and the $j-th$ value of SNR;
- N_{SNR} is the total number of considered SNR values.

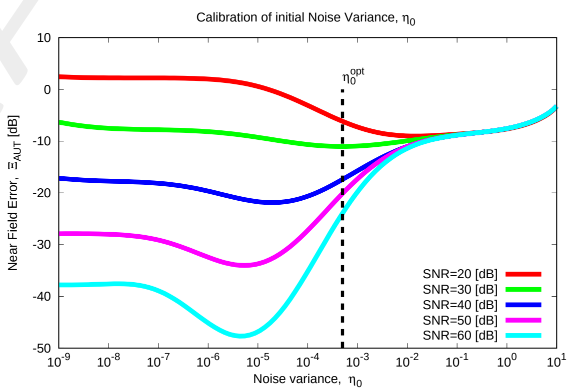

Figure 3: Initial noise variance η_0 calibration considering $H_{meas} = 1\,[\lambda]$ and $M = 16$.

The resulting optimum value for the initial noise variance is:

$$\eta_0^{\mathbf{opt}} = \mathbf{5} \times \mathbf{10^{-4}}.$$

1.1.1 Height of the measurement region $\mathbf{H_{meas}} = \mathbf{5}\,[\lambda]$

Original (*OMP*) MbD parameters

- Max. number of iterations of the OMP algorithm : $I = \{1; 2; 3; ...; 10\}$;
- Selected iteration to report the results: $I = 2$; this choice is justified by the fact that at this iteration the *OMP* algorithm reaches the best near field error as shown in the following Fig. 4.

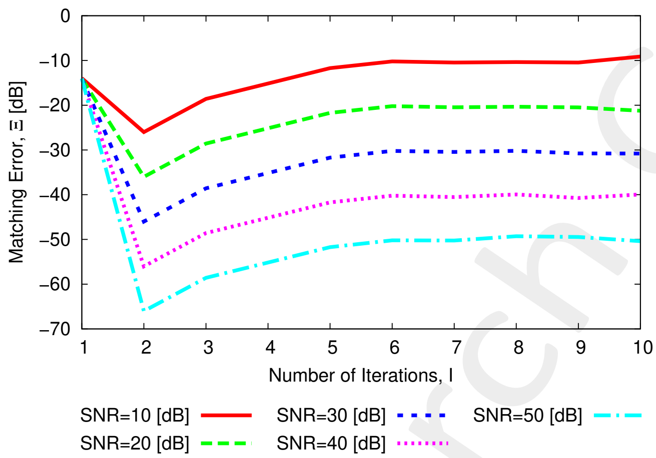

Figure 4: Behaviour of the near-field matching error versus the number of *OMP* iterations, I.

Evaluation of the Truncation Error from Actual Near-Field Data

In order to evaluate the truncation error, in the following figure is presented a visual comparison of the near-field radiated by the *AUT* measured over the full interpolation region and on the truncated region, as well as the corresponding far-field patterns obtained with NF-FF transformation. The truncated near-field has been obtained as follows:

$$E_{tr}(\varphi, z) = \begin{cases} E(\varphi, z) & if \quad -\frac{H_{meas}}{2} \leq z \leq \frac{H_{meas}}{2} \\ 0 & otherwise \end{cases} \quad ; -\frac{H_{int}}{2} \leq z \leq \frac{H_{int}}{2} \tag{2}$$

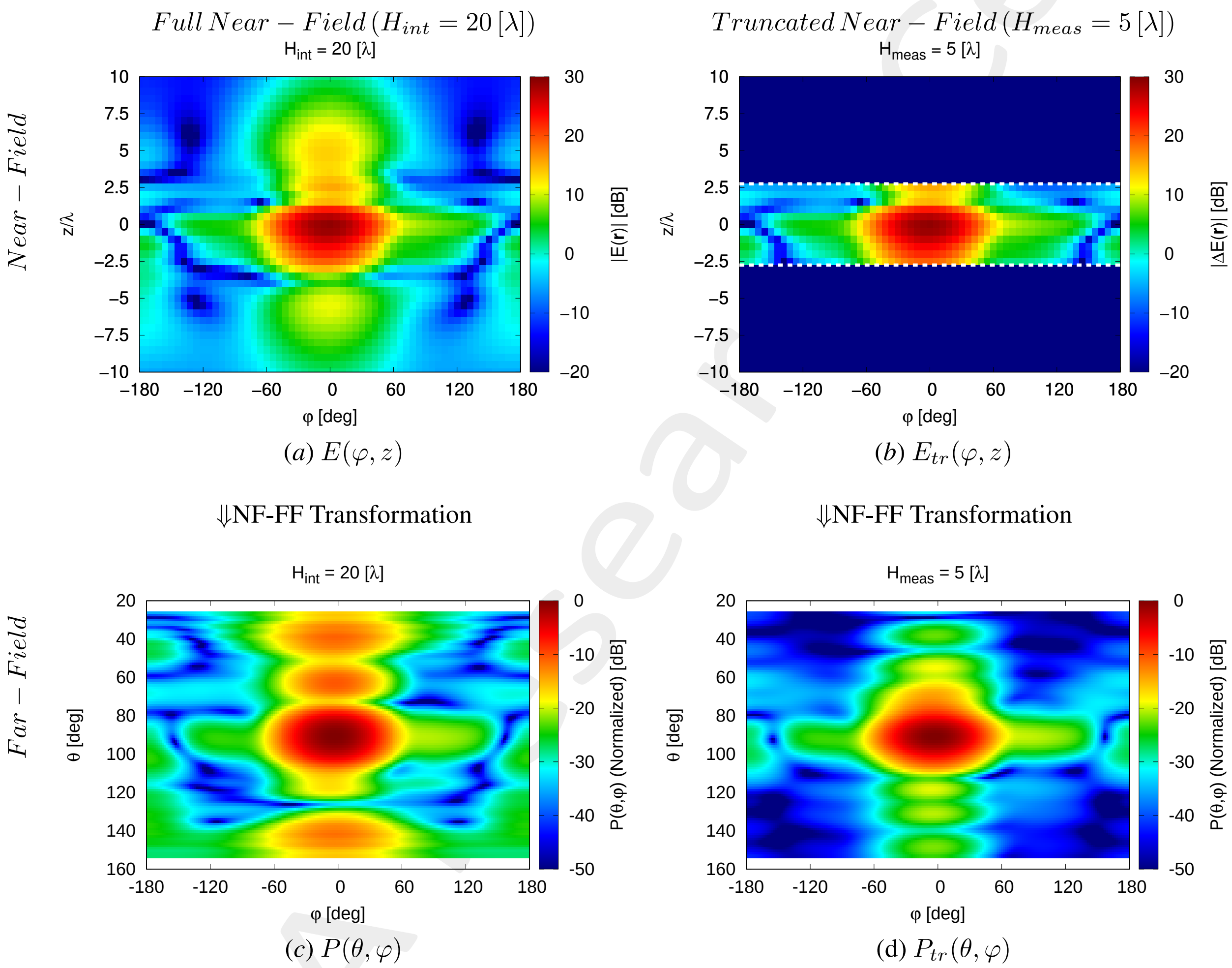

Figure 5: $H_{meas} = 5\,[\lambda]$ - $(a)(b)$ Near-field and $(c)(d)$ far-field patterns obtained via NF-FF transformation for the actual *AUT*.

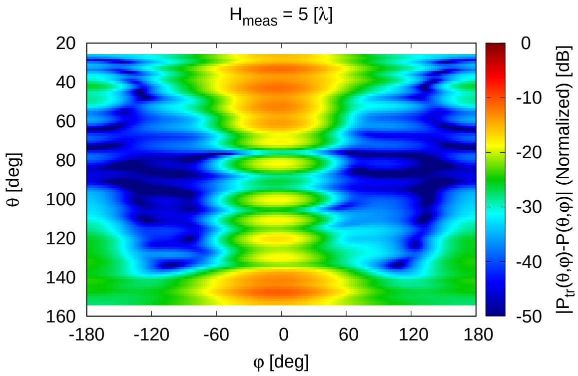

Figure 6: $H_{meas} = 5\,[\lambda]$ - Difference between the full and the truncated far-fields, $|P(\theta,\varphi) - P_{tr}(\theta,\varphi)|$.

Near-Field Error

The comparison, in terms of near field error, between the original (*OMP*) and the alternative (*BCS*) MbD is reported in the following Fig. 7:

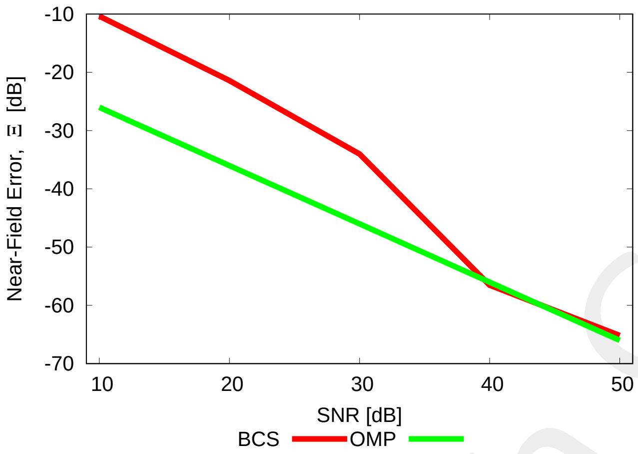

Figure 7: Near Field Error comparison between original (*OMP*) and alternative (*BCS*) MbD for different SNR values

$SNR\,[dB]$	*Near Field Error,* Ξ $[dB]$	
	BCS	OMP
50	-65.18	-66.01
40	-56.53	-56.01
30	-34.03	-46.01
20	-21.43	-36.01
10	-10.35	-26.01

Table II: Near Field Errors obtained by the original (*OMP*) and alternative (*BCS*) MbD

Observations

By observing the reported results it is possible to point out that the *OMP* algorithm outperforms the other one almost all over the entire range of *SNR* values. In particular:

- the *OMP* obtains satisfactory results already at $SNR = 10\,[dB]$ where $\Xi < -25\,[dB]$ and then its error decreases linearly with the increase of the SNR;
- the *BCS* results start to be good at $SNR = 30\,[dB]$ since the error goes below $-25\,[dB]$; moving from $SNR = 30\,[dB]$ to $SNR = 40\,[dB]$ there is a remarkable result improvement and then the performance continue to enhance with the increase of the SNR so that for $SNR \geq 40\,[dB]$ the *BCS* results are comparable to those of the *OMP*.

Estimated Near-Field

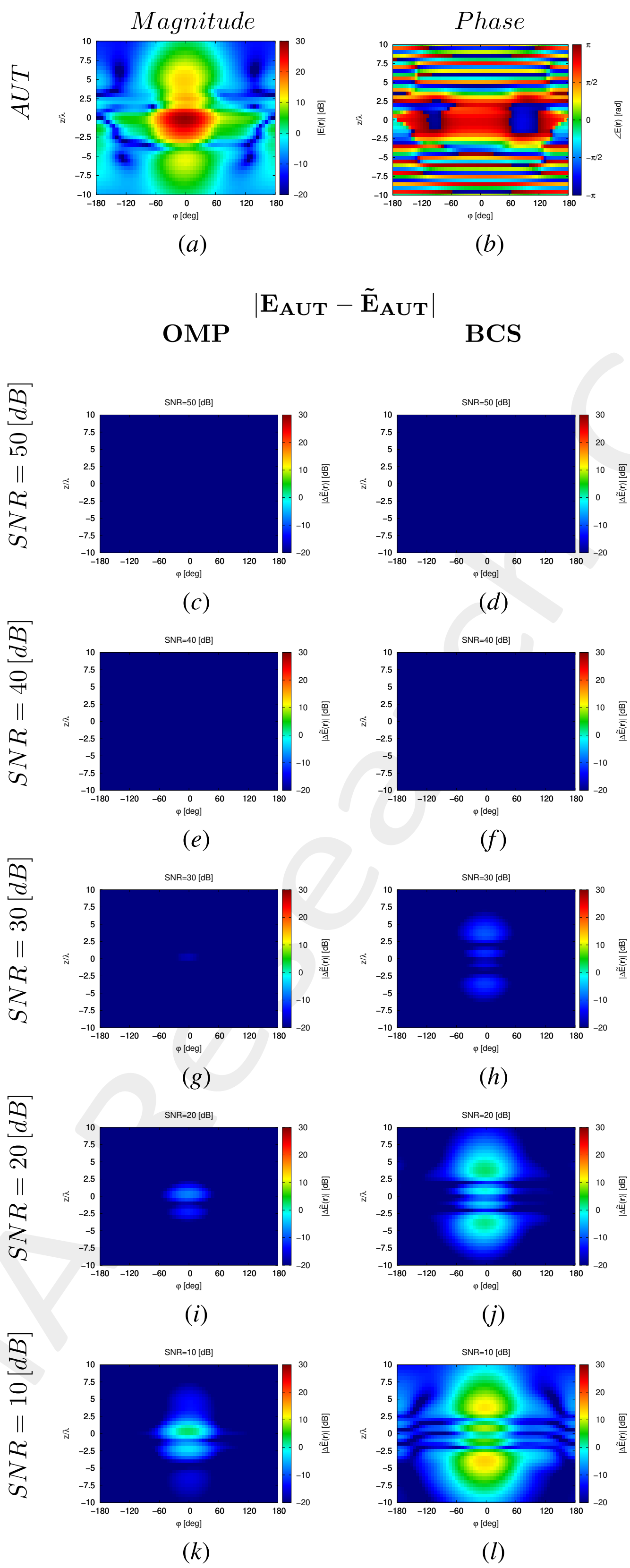

Figure 8: Magnitude difference between the actual and estimated $2-D$ near-field pattern when processing noisy measurements at different SNRs.

Estimated Far-Field

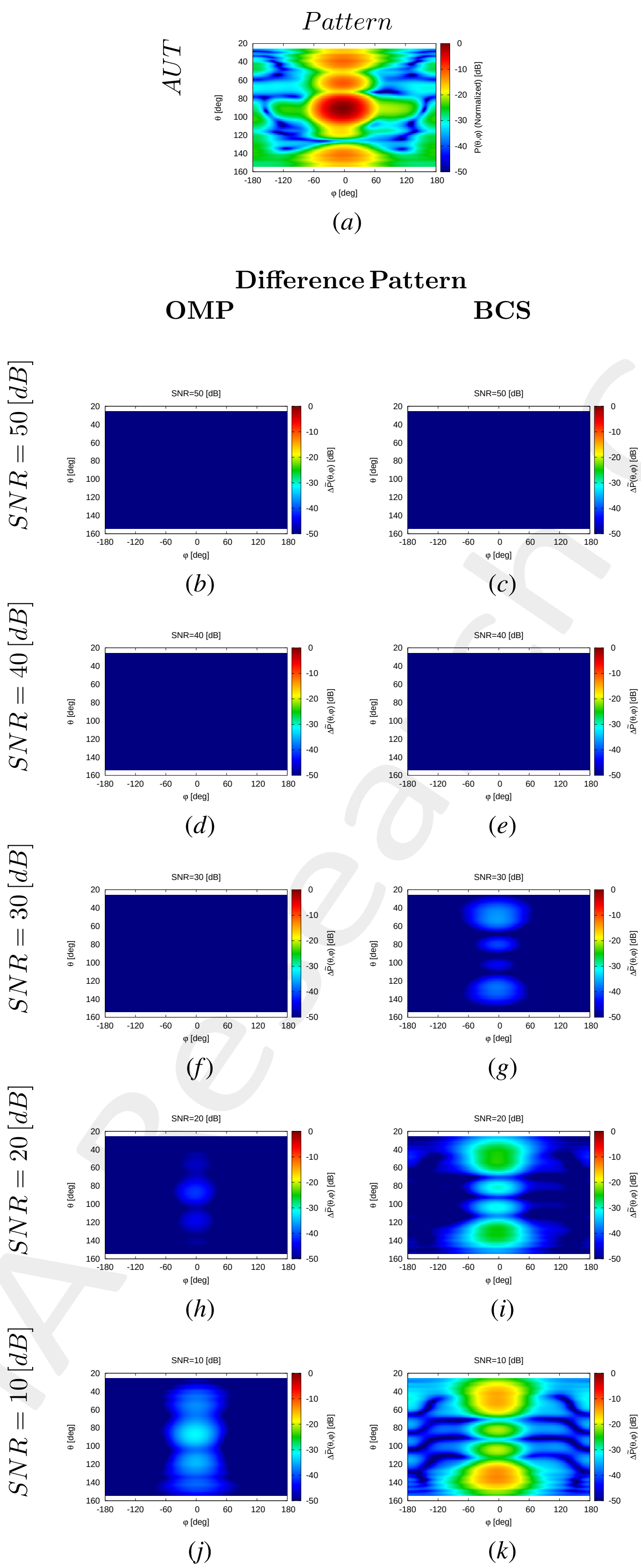

Figure 9: Difference between the actual and estimated $2-D$ far-field pattern when processing noisy measurements at different $SNRs$.

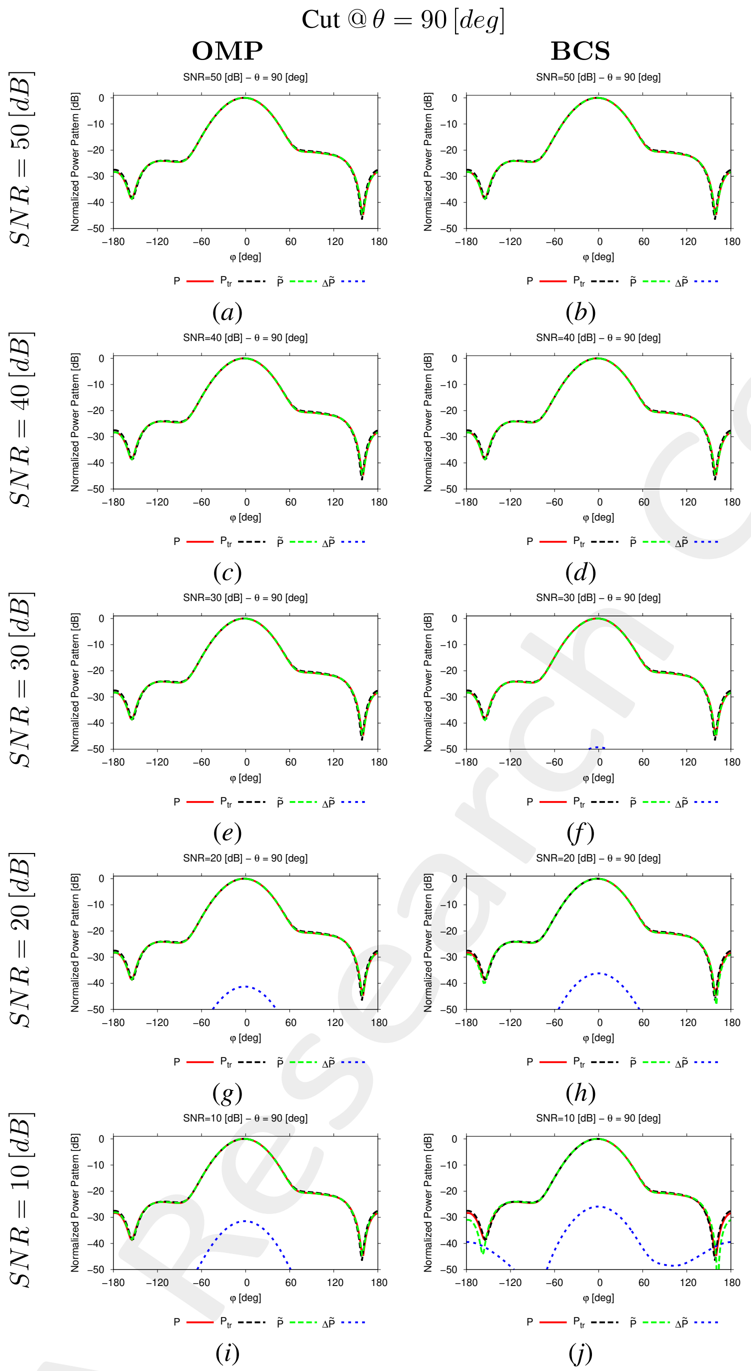

Figure 10: $1-D$ cuts of the estimated far-field pattern (obtained through near-to-far-field transformation from the estimated near-field patterns) under several noisy conditions

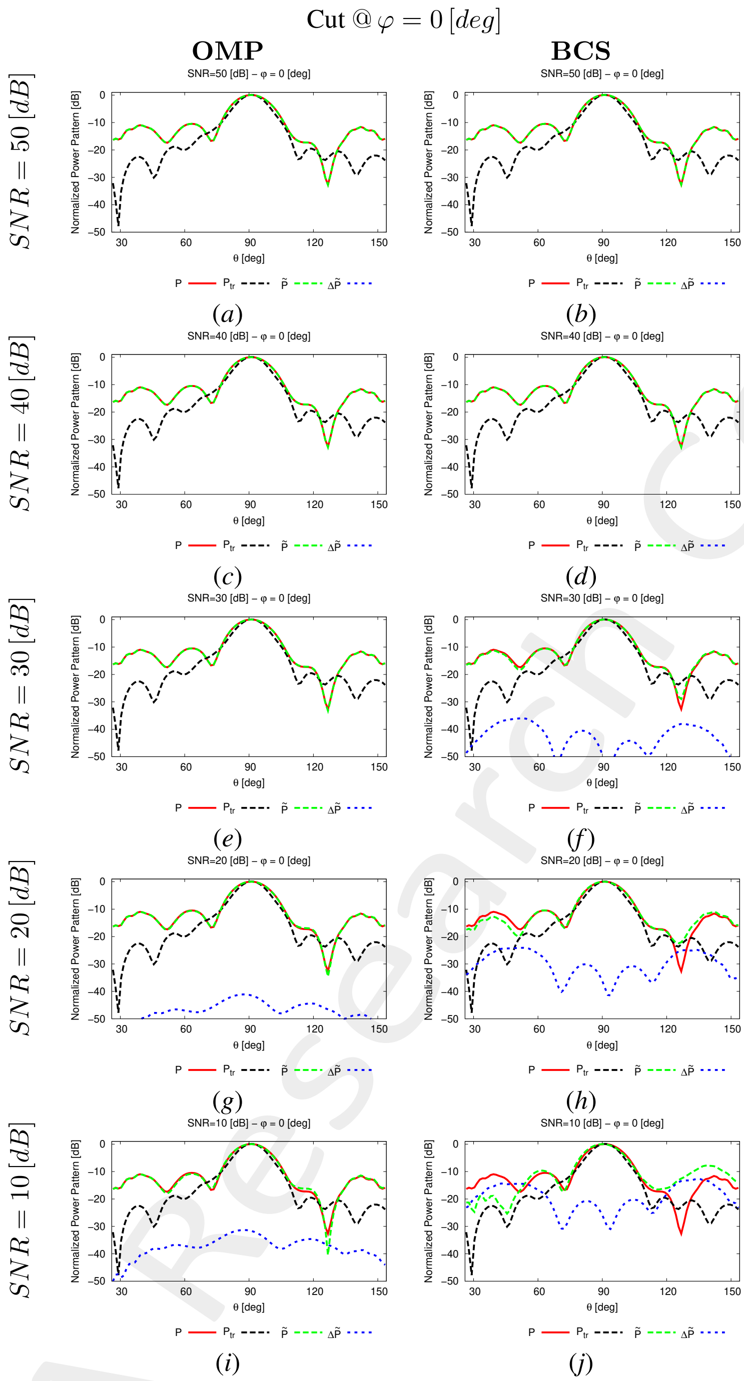

Figure 11: $1-D$ cuts of the estimated far-field pattern (obtained through near-to-far-field transformation from the estimated near-field patterns) under several noisy conditions

$SNR\,[dB]$	$Far-Field\ Error,\ \chi\ [dB]$	
	BCS	OMP
50	-64.61	-67.58
40	-58.51	-57.62
30	-31.02	-47.65
20	-18.00	-37.71
10	-6.81	-27.92

Table III: Far-field matching error between the actual and estimated AUT patterns (both obtained through near-to-far-field transformation from the corresponding near-field patterns) under several noisy conditions.

Estimated Coefficients

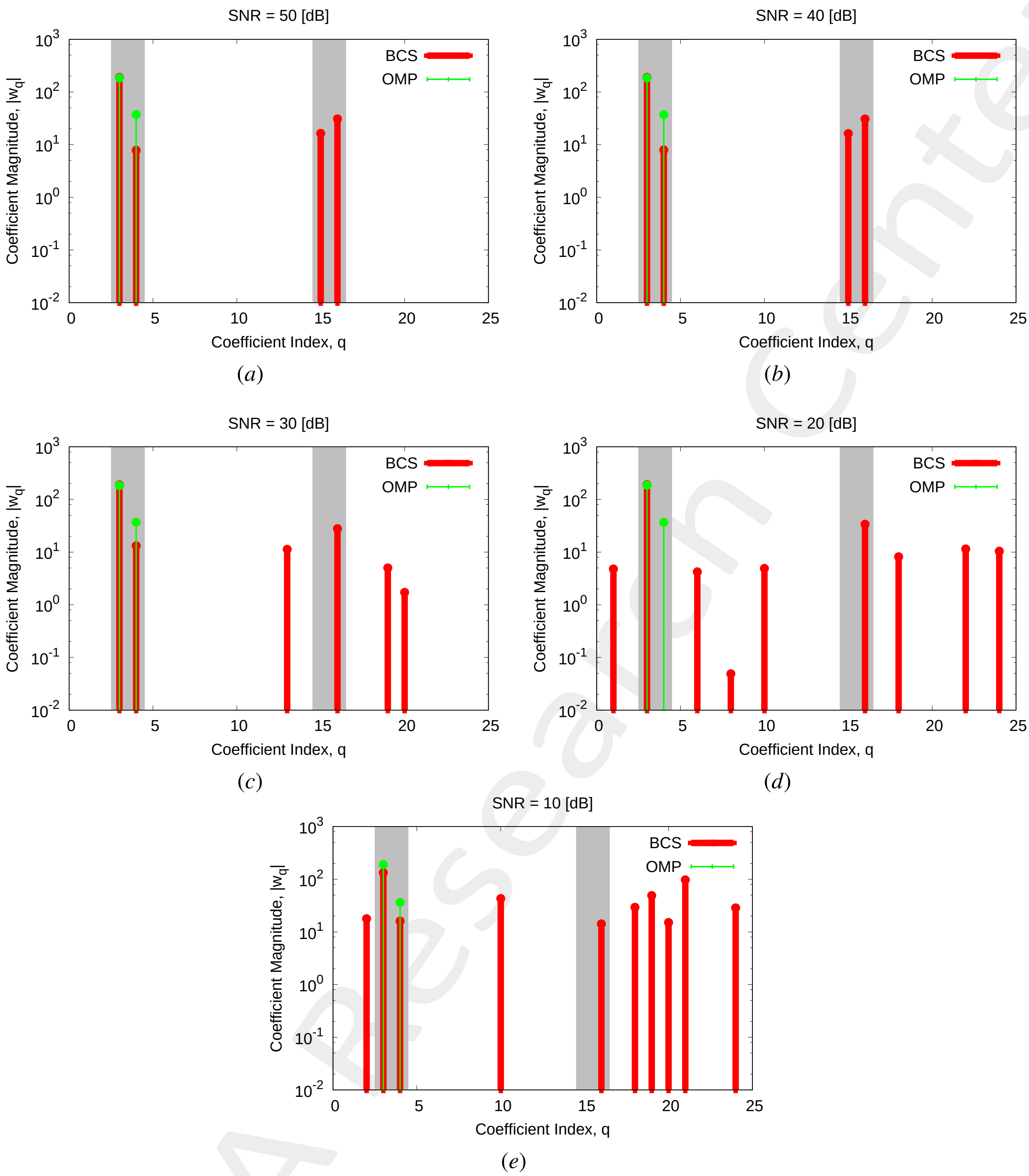

Figure 12: Coefficient comparison between original (*OMP*) and alternative (*BCS*) MbD : (*a*) $SNR = 50\,[dB]$, (*b*) $SNR = 40\,[dB]$, (*c*) $SNR = 30\,[dB]$, (*d*) $SNR = 20\,[dB]$, (*e*) $SNR = 10\,[dB]$

Observations

The considered *AUT* is characterized by an excitation magnitude and phase of the second subarray (i.e., $\nu^{(2)} = 0.43$ and $\gamma^{(2)} = \frac{\pi}{3}\,[rad]$):

- the *OMP* selects always the same two vectors corresponding to the magnitude failure actually affecting the *AUT* and none of those associated to the phase failure;
- the *BCS* algorithm is able to identify both the failures affecting the AUT even if the failure detections, at $10\,[dB] \leq SNR \leq 30\,[dB]$, are not precise since the method selects also vectors not connected to the actual failures and it

doesn't pick all the vectors of the failures affecting the *AUT*. For $SNR \geq 40\,[dB]$ the BCS precisely selects all the basis functions associated to the failures affecting the *AUT*.

Computational times

- Δt_{Sim}: Time required to simulate the K *AUT* configurations used to build the $(T \times K)$ "pattern matrix";
- Δt_{SVD}: Time required to perform the *SVD* of the $(T \times K)$ "pattern matrix";
- $\Delta t_{MbE}^{OMP/BCS}$: (Mean) Time required by the Measurement-by-Example tool to read the *SVD* output and perform the estimation of the *AUT* radiated field.

Δt_{Sim} $[sec]$	4.72×10^{4}
Δt_{SVD} $[sec]$	1.79×10^{2}
Δt_{MbE}^{BCS} $[sec]$	2.67×10^{-1}
Δt_{MbE}^{OMP} $[sec]$	1.93×10^{-3}

Table IV: Computational times

Remarks

- Given that the number of simulated *AUT*s is $K = S \times (F^{(s)} + P^{(s)}) = 84$, the average per-*AUT* simulation time is

$$\Delta t_{FEKO} \simeq \frac{\Delta t_{Sim}}{K} = \frac{4.72 \times 10^{4}}{84} [sec] = 5.62 \times 10^{2} [sec]$$

1.1.2 Height of the measurement region $\mathbf{H_{meas}} = 4\,[\lambda]$

Original (*OMP*) MbD parameters

- Max. number of iterations of the OMP algorithm : $I = \{1; 2; 3; ...; 10\}$;
- Selected iteration to report the results: $I = 3$; this choice is justified by the fact that at this iteration the *OMP* algorithm reaches the best near field error as shown in the following Fig. 13.

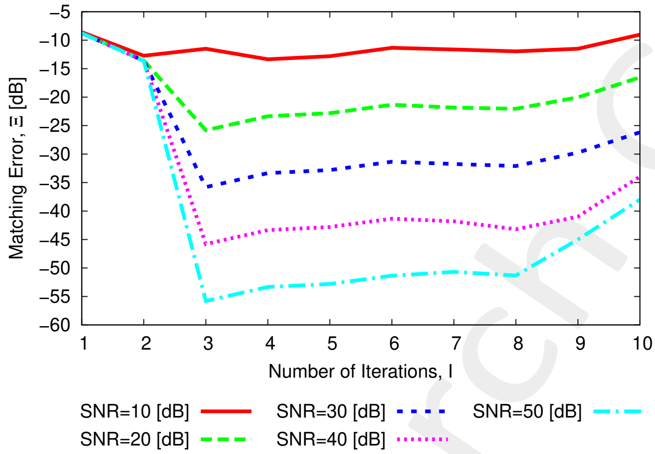

Figure 13: Behaviour of the near-field matching error versus the number of *OMP* iterations, I.

Evaluation of the Truncation Error from Actual Near-Field Data

In order to evaluate the truncation error, in the following figure is presented a visual comparison of the near-field radiated by the *AUT* measured over the full interpolation region and on the truncated region, as well as the corresponding far-field patterns obtained with NF-FF transformation. The truncated near-field has been obtained as follows:

$$E_{tr}(\varphi, z) = \begin{cases} E(\varphi, z) & if \quad -\frac{H_{meas}}{2} \leq z \leq \frac{H_{meas}}{2} \\ 0 & otherwise \end{cases} \quad ; -\frac{H_{int}}{2} \leq z \leq \frac{H_{int}}{2}$$

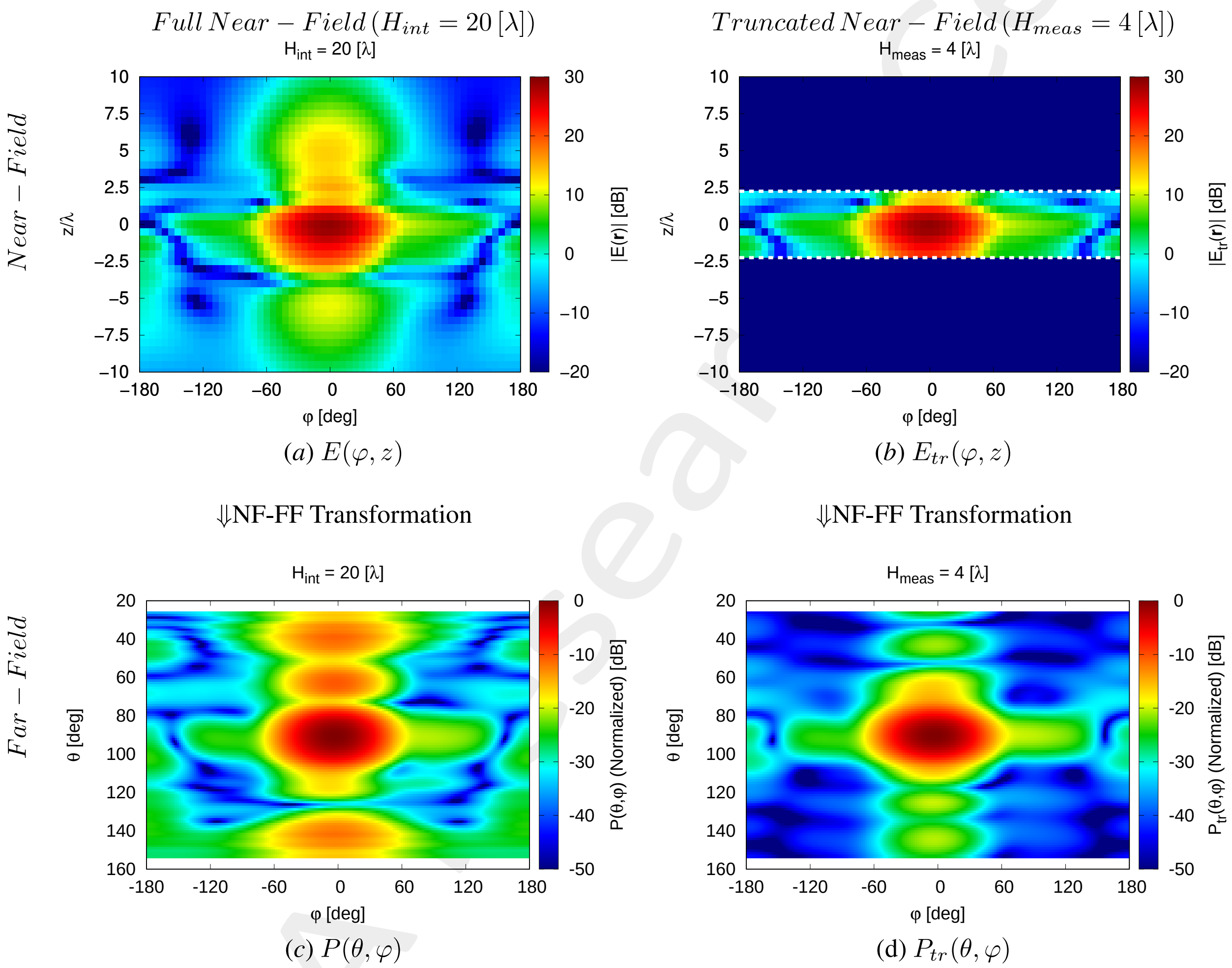

Figure 14: $H_{meas} = 4\,[\lambda]$ - $(a)(b)$ Near-field and $(c)(d)$ far-field patterns obtained via NF-FF transformation for the actual *AUT*.

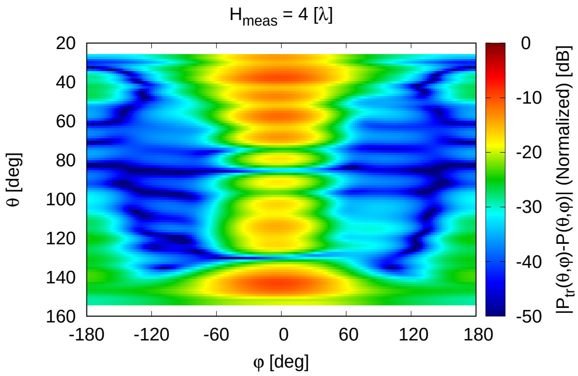

Figure 15: $H_{meas} = 4\,[\lambda]$ - Difference between the full and the truncated far-fields, $|P(\theta,\varphi) - P_{tr}(\theta,\varphi)|$.

Near-Field Error

The comparison, in terms of near field error, between the original (*OMP*) and the alternative (*BCS*) MbD is reported in the following Fig. 16:

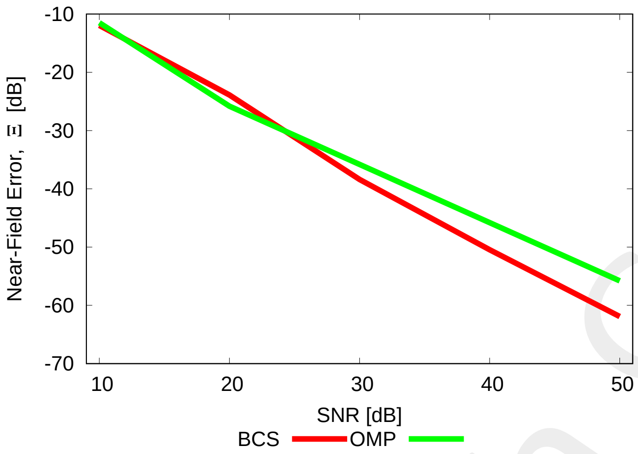

Figure 16: Near Field Error comparison between original (*OMP*) and alternative (*BCS*) MbD for different SNR values

$SNR\,[dB]$	*Near Field Error,* Ξ $[dB]$	
	BCS	OMP
50	-61.91	-55.79
40	-50.45	-45.80
30	-38.39	-35.80
20	-23.90	-25.81
10	-11.94	-11.49

Table V: Near Field Errors obtained by the original (*OMP*) and alternative (*BCS*) MbD

Observations

By observing the reported results it is possible to point out that :

- the *OMP* error decreases linearly with the increase of the SNR reaching good performance ($\Xi \leq -25\,[dB]$) starting from $SNR = 20\,[dB]$;
- the *BCS* results are are not good until for $SNR < 30\,[dB]$ but similar to those of the *OMP*; however, starting from $SNR = 30\,[dB]$ the *BCS* reaches lower errors than the *OMP* ones.

Estimated Near-Field

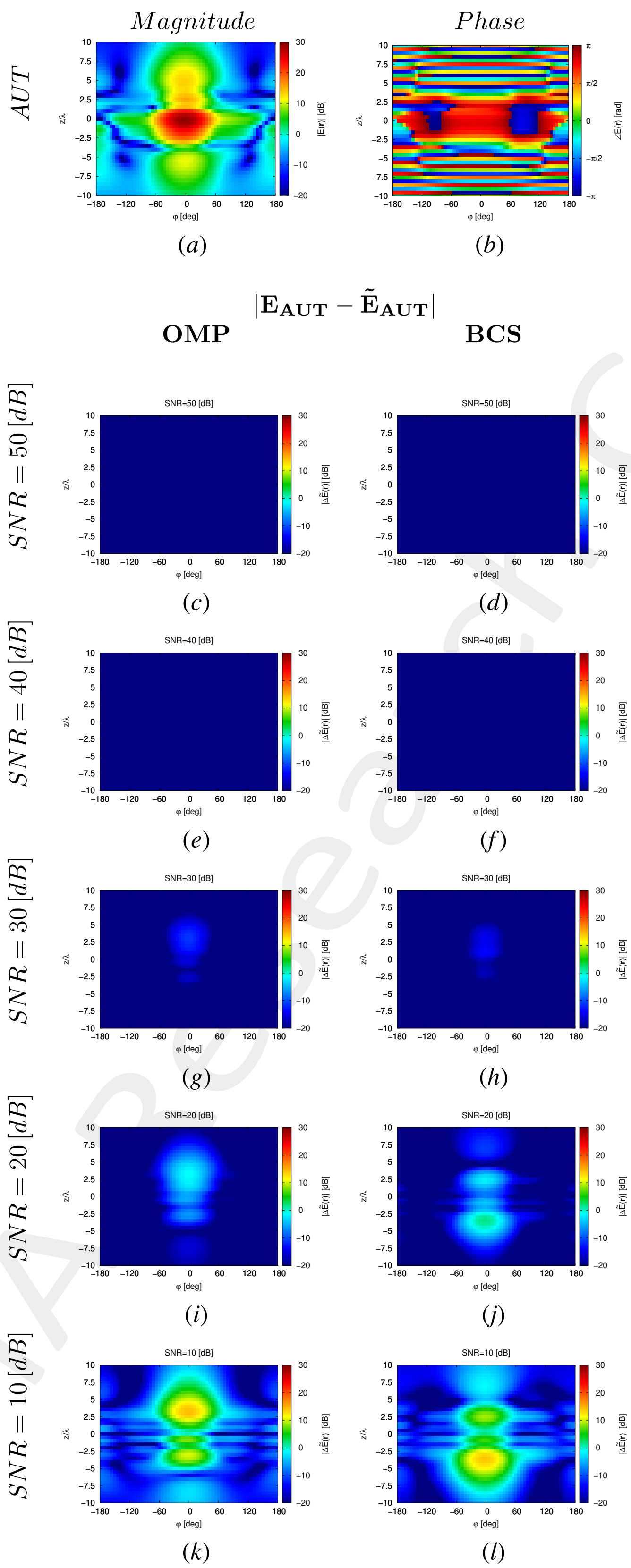

Figure 17: Magnitude difference between the actual and estimated $2-D$ near-field pattern when processing noisy measurements at different SNRs.

Estimated Far-Field

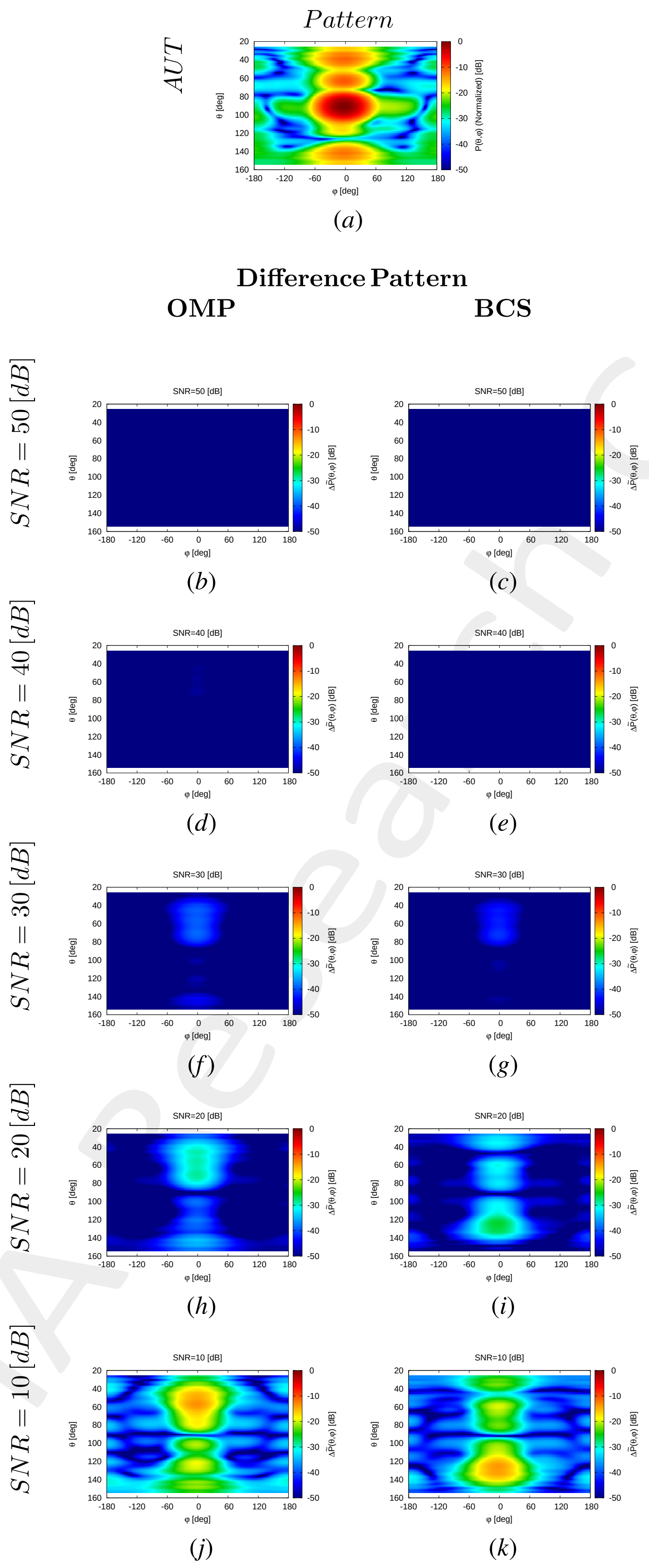

Figure 18: Difference between the actual and estimated $2-D$ far-field pattern when processing noisy measurements at different SNRs.

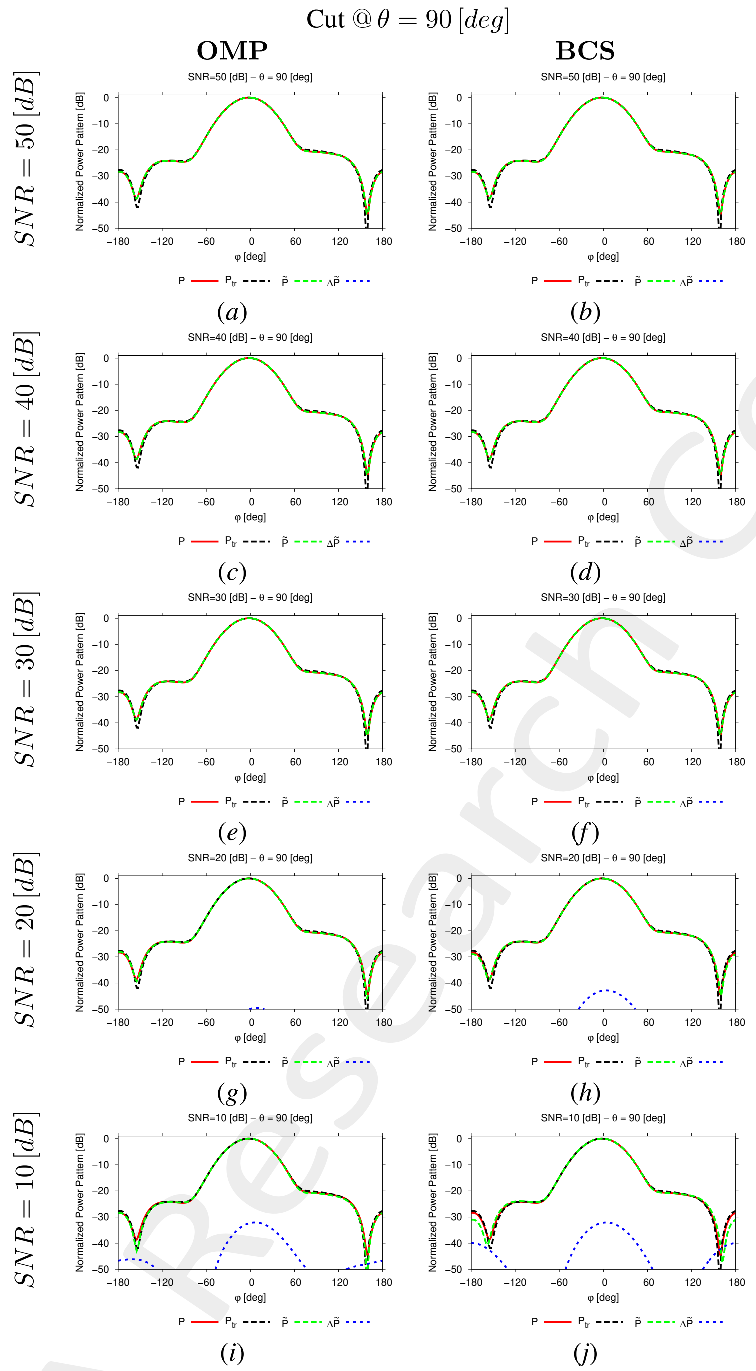

Figure 19: $1-D$ cuts of the estimated far-field pattern (obtained through near-to-far-field transformation from the estimated near-field patterns) under several noisy conditions

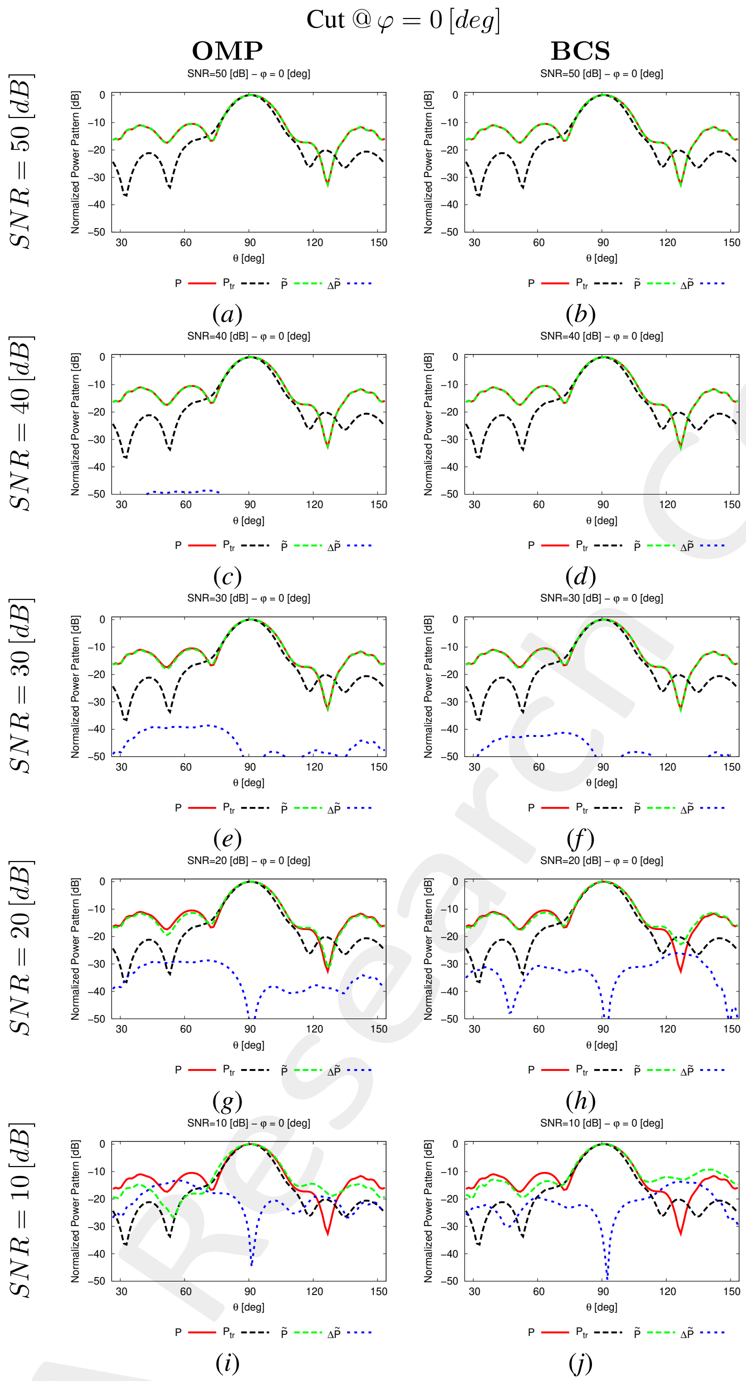

Figure 20: $1-D$ cuts of the estimated far-field pattern (obtained through near-to-far-field transformation from the estimated near-field patterns) under several noisy conditions

$SNR\,[dB]$	$Far-Field\ Error,\ \chi\ [dB]$	
	BCS	OMP
50	-60.59	-55.79
40	-49.10	-45.80
30	-36.58	-35.80
20	-21.79	-25.81
10	-9.88	-11.49

Table VI: Far-field matching error between the actual and estimated AUT patterns (both obtained through near-to-far-field transformation from the corresponding near-field patterns) under several noisy conditions.

Estimated Coefficients

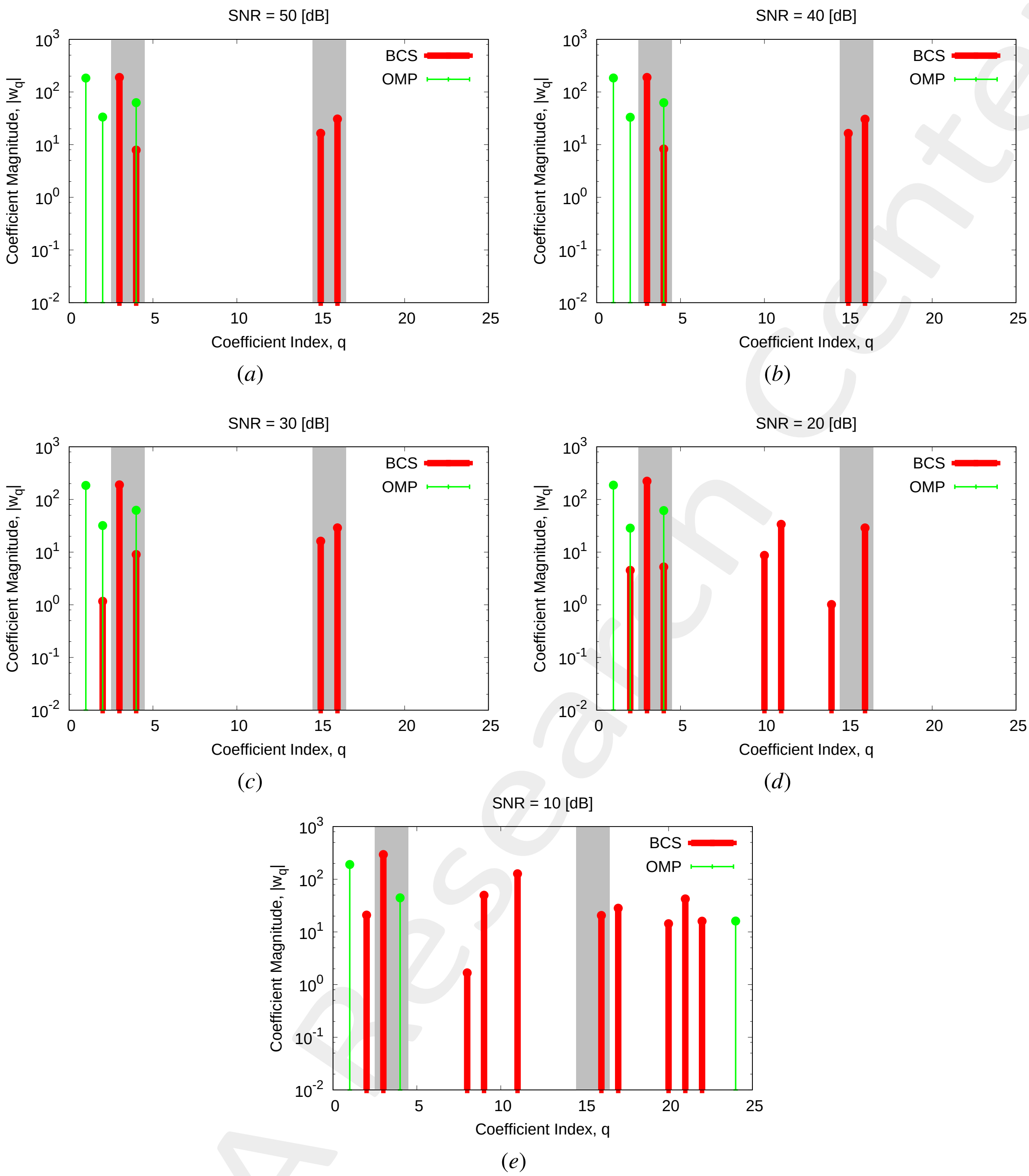

Figure 21: Coefficient comparison between original (*OMP*) and alternative (*BCS*) MbD : (*a*) $SNR = 50\,[dB]$, (*b*) $SNR = 40\,[dB]$, (*c*) $SNR = 30\,[dB]$, (*d*) $SNR = 20\,[dB]$, (*e*) $SNR = 10\,[dB]$

Observations

The considered *AUT* is characterized by an excitation magnitude and phase of the second subarray (i.e., $\nu^{(2)} = 0.43$ and $\gamma^{(2)} = \frac{\pi}{3}\,[rad]$):

- the *OMP* solver, except at $SNR = 10\,[dB]$, always selects the same three vectors corresponding to magnitude failures but just one of them is associated to the magnitude failure actually affecting the *AUT*.
- the *BCS* algorithm is able to identify both the failures affecting the AUT even if the failure detections are not precise at low $SNRs$ since the method selects also vectors not connected to the actual failures and it doesn't pick

all the vectors of the failures affecting the *AUT*. In particular, the *BCS* correctly identify both the failures affecting the *AUT* starting from $SNR = 40\,[dB]$.

Computational times

- Δt_{Sim}: Time required to simulate the K *AUT* configurations used to build the $(T \times K)$ "pattern matrix";
- Δt_{SVD}: Time required to perform the *SVD* of the $(T \times K)$ "pattern matrix";
- $\Delta t_{MbE}^{OMP/BCS}$: (Mean) Time required by the Measurement-by-Example tool to read the *SVD* output and perform the estimation of the *AUT* radiated field.

Δt_{Sim} $[sec]$	4.72×10^4
Δt_{SVD} $[sec]$	1.79×10^2
Δt_{MbE}^{BCS} $[sec]$	3.14×10^{-1}
Δt_{MbE}^{OMP} $[sec]$	2.11×10^{-3}

Table VII: Computational times

Remarks

- Given that the number of simulated *AUT*s is $K = S \times (F^{(s)} + P^{(s)}) = 84$, the average per-*AUT* simulation time is

$$\Delta t_{FEKO} \simeq \frac{\Delta t_{Sim}}{K} = \frac{4.72 \times 10^4}{84} [sec] = 5.62 \times 10^2 \, [sec]$$

More information on the topics of this document can be found in the following list of references.

References

[1] M. Salucci, N. Anselmi, M. D. Migliore and A. Massa, "A bayesian compressive sensing approach to robust near-field antenna characterization," *IEEE Trans. Antennas Propag.*, vol. 70, no. 9, pp. 8671-8676, Sep. 2022 (DOI: 10.1109/TAP.2022.3177528).

[2] B. Li, M. Salucci, W. Tang, and P. Rocca, "Reliable field strength prediction through an adaptive total-variation CS technique," *IEEE Antennas Wirel. Propag. Lett.*, vol. 19, no. 9, pp. 1566-1570, Sep. 2020.

[3] M. Salucci, M. D. Migliore, P. Rocca, A. Polo, and A. Massa, "Reliable antenna measurements in a near-field cylindrical setup with a sparsity promoting approach," *IEEE Trans. Antennas Propag.*, vol. 68, no. 5, pp. 4143-4148, May 2020.

[4] G. Oliveri, M. Salucci, N. Anselmi, and A. Massa, "Compressive sensing as applied to inverse problems for imaging: theory, applications, current trends, and open challenges," *IEEE Antennas Propag. Mag. - Special Issue on "Electromagnetic Inverse Problems for Sensing and Imaging*," vol. 59, no. 5, pp. 34-46, Oct. 2017.

[5] A. Massa, P. Rocca, and G. Oliveri, "Compressive sensing in electromagnetics - A review," *IEEE Antennas Propag. Mag.*, pp. 224-238, vol. 57, no. 1, Feb. 2015.

[6] A. Massa and F. Texeira, "Guest-Editorial: Special Cluster on Compressive Sensing as Applied to Electromagnetics," *IEEE Antennas Wirel. Propag. Lett.*, vol. 14, pp. 1022-1026, 2015.

[7] G. Oliveri, N. Anselmi, M. Salucci, L. Poli, and A. Massa, "Compressive sampling-based scattering data acquisition in microwave imaging," *J. Electromagn. Waves Appl*, vol. 37, no. 5, 693-729, March 2023 (DOI: 10.1080/09205071.2023.2188263).

[8] G. Oliveri, L. Poli, N. Anselmi, M. Salucci, and A. Massa, "Compressive sensing-based Born iterative method for tomographic imaging," *IEEE Trans. Microw. Theory Techn.*, vol. 67, no. 5, pp. 1753-1765, May 2019.

[9] M. Salucci, L. Poli, and G. Oliveri, "Full-vectorial 3D microwave imaging of sparse scatterers through a multi-task Bayesian compressive sensing approach," *J. Imaging*, vol. 5, no. 1, pp. 1-24, Jan. 2019.

[10] M. Salucci, A. Gelmini, L. Poli, G. Oliveri, and A. Massa, "Progressive compressive sensing for exploiting frequency-diversity in GPR imaging," *J. Electromagn. Waves Appl.*, vol. 32, no. 9, pp. 1164-1193, 2018.

[11] N. Anselmi, L. Poli, G. Oliveri, and A. Massa, "Iterative multi-resolution bayesian CS for microwave imaging," *IEEE Trans. Antennas Propag.*, vol. 66, no. 7, pp. 3665-3677, Jul. 2018.

[12] N. Anselmi, G. Oliveri, M. A. Hannan, M. Salucci, and A. Massa, "Color compressive sensing imaging of arbitrary-shaped scatterers," *IEEE Trans. Microw. Theory Techn.*, vol. 65, no. 6, pp. 1986-1999, Jun. 2017.

[13] N. Anselmi, G. Oliveri, M. Salucci, and A. Massa, "Wavelet-based compressive imaging of sparse targets" *IEEE Trans. Antennas Propag.*, vol. 63, no. 11, pp. 4889-4900, Nov. 2015.

[14] G. Oliveri, P.-P. Ding, and L. Poli, "3D crack detection in anisotropic layered media through a sparseness-regularized solver," *IEEE Antennas Wirel. Propag. Lett.*, vol. 14, pp. 1031-1034, 2015.

[15] L. Poli, G. Oliveri, P.-P. Ding, T. Moriyama, and A. Massa, "Multifrequency Bayesian compressive sensing methods for microwave imaging," *J. Opt. Soc. Am. A*, vol. 31, no. 11, pp. 2415-2428, 2014.

[16] G. Oliveri, N. Anselmi, and A. Massa, "Compressive sensing imaging of non-sparse 2D scatterers by a total-variation approach within the Born approximation," *IEEE Trans. Antennas Propag.*, vol. 62, no. 10, pp. 5157-5170, Oct. 2014.

[17] L. Poli, G. Oliveri, F. Viani, and A. Massa, "MT-BCS-based microwave imaging approach through minimum-norm current expansion," *IEEE Trans. Antennas Propag.*, vol. 61, no. 9, pp. 4722-4732, Sep. 2013.

[18] F. Viani, L. Poli, G. Oliveri, F. Robol, and A. Massa, "Sparse scatterers imaging through approximated multitask compressive sensing strategies," *Microwave Opt. Technol. Lett.*, vol. 55, no. 7, pp. 1553-1558, Jul. 2013.

[19] L. Poli, G. Oliveri, P. Rocca, and A. Massa, "Bayesian compressive sensing approaches for the reconstruction of two-dimensional sparse scatterers under TE illumination," *IEEE Trans. Geosci. Remote Sensing*, vol. 51, no. 5, pp. 2920-2936, May 2013.

[20] P. Rocca, N. Anselmi, M. A. Hannan, and A. Massa, "Conical frustum multi-beam phased arrays for air traffic control radars," *Sensors*, vol. 22, no. 19, 7309, pp. 1-18, 2022 (DOI: 10.3390/s22197309)

[21] F. Zardi, G. Oliveri, M. Salucci, and A. Massa, "Minimum-complexity failure correction in linear arrays via compressive processing," *IEEE Trans. Antennas Propag.*, vol. 69, no. 8, pp. 4504-4516, Aug. 2021.

[22] N. Anselmi, G. Gottardi, G. Oliveri, and A. Massa, "A total-variation sparseness-promoting method for the synthesis of contiguously clustered linear architectures," *IEEE Trans. Antennas Propag.*, vol. 67, no. 7, pp. 4589-4601, Jul. 2019.

[23] M. Salucci, A. Gelmini, G. Oliveri, and A. Massa, "Planar arrays diagnosis by means of an advanced Bayesian compressive processing," *IEEE Trans. Antennas Propag.*, vol. 66, no. 11, pp. 5892-5906, Nov. 2018.

[24] L. Poli, G. Oliveri, P. Rocca, M. Salucci, and A. Massa, "Long-Distance WPT Unconventional Arrays Synthesis," *J. Electromagn. Waves Appl.*, vol. 31, no. 14, pp. 1399-1420, Jul. 2017.

[25] G. Oliveri, M. Salucci, and A. Massa, "Synthesis of modular contiguously clustered linear arrays through a sparseness-regularized solver," *IEEE Trans. Antennas Propag.*, vol. 64, no. 10, pp. 4277-4287, Oct. 2016.

[26] M. Carlin, G. Oliveri, and A. Massa, "Hybrid BCS-deterministic approach for sparse concentric ring isophoric arrays," *IEEE Trans. Antennas Propag.*, vol. 63, no. 1, pp. 378-383, Jan. 2015.

[27] G. Oliveri, E. T. Bekele, F. Robol, and A. Massa, "Sparsening conformal arrays through a versatile BCS-based method," *IEEE Trans. Antennas Propag.*, vol. 62, no. 4, pp. 1681-1689, Apr. 2014.

[28] F. Viani, G. Oliveri, and A. Massa, “Compressive sensing pattern matching techniques for synthesizing planar sparse arrays,” *IEEE Trans. Antennas Propag.*, vol. 61, no. 9, pp. 4577-4587, Sept. 2013.

[29] P. Rocca, M. A. Hannan, M. Salucci, and A. Massa, “Single-snapshot DoA estimation in array antennas with mutual coupling through a multi-scaling BCS strategy,” *IEEE Trans. Antennas Propag.*, vol. 65, no. 6, pp. 3203-3213, Jun. 2017.

[30] M. Carlin, P. Rocca, G. Oliveri, F. Viani, and A. Massa, “Directions-of-arrival estimation through Bayesian Compressive Sensing strategies,” *IEEE Trans. Antennas Propag.*, vol. 61, no. 7, pp. 3828-3838, Jul. 2013.

[31] M. Carlin, P. Rocca, G. Oliveri, and A. Massa, “Bayesian compressive sensing as applied to directions-of-arrival estimation in planar arrays," *J. Electromagn. Waves Appl.*, vol.2013, pp.1-12, 2013 (DOI :10.1155/2013/245867).